

ON THE REDSHIFT EVOLUTION OF MG II ABSORPTION SYSTEMS

JEREMY L. TINKER¹ & HSIAO-WEN CHEN²

¹Berkeley Center for Cosmological Physics, University of California-Berkeley

²Department of Astronomy and Astrophysics & Kavli Institute for Cosmological Physics, University of Chicago

Draft version September 15, 2021

ABSTRACT

We use a halo occupation approach to connect Mg II absorbers to dark matter halos as a function of redshift. Using the model constructed in Tinker & Chen (2008), we parameterize the conditional probability of an absorber of equivalent width W_r being produced by a halo of mass M_h at a given redshift, $P(W_r|M_h, z)$. We constrain the free parameters of the model by matching the observed statistics of Mg II absorbers: the frequency function $f(W_r)$, the redshift evolution $n(z)$, and the clustering bias b_W . The redshift evolution of $W_r \geq 1$ absorbers increases from $z = 0.4$ to $z = 2$, while the total halo cross section decreases monotonically with redshift. This discrepancy can only be explained if the gaseous halos evolve with respect to their host halos. We make predictions for the clustering bias of absorbers as a function of redshift under different evolutionary scenarios, eg, the gas cross section per halo evolves or the halo mass scale of absorbers changes. We demonstrate that the relative contribution of these scenarios may be constrained by measurements of absorber clustering at $z \gtrsim 1$ and $z \sim 0.1$. If we further assume a redshift-independent mass scale for efficient shock heating of halo gas of $M_{\text{crit}} = 10^{11.5} h^{-1} M_\odot$, absorber evolution is predominantly caused by a changing halo mass scale of absorbers. Our model predicts that strong absorbers always arise in $\sim M_{\text{crit}}$ halos, independent of redshift, but the mass scale of weak absorbers decreases by 2 dex from $0 < z < 2$. Thus, the measured anti-correlation of clustering bias and W_r should flatten by $z \sim 1.5$.

Subject headings: cosmology—intergalactic medium—quasars: absorption lines—dark matter: halos

1. INTRODUCTION

Absorption lines in the spectra of quasars reflect the presence of gas intersected along the lines of sight to the QSOs. A subset of these absorption lines systems, i.e., Mg II, CIV, Lyman-limit systems, are created when a line of sight passes through a dark matter halo that contains cool or warm gas. The presence of Mg⁺ indicates that the gas is photoionized with a temperature near 10^4 K. The connection between Mg II absorbers and dark matter halos is well established: Mg II absorbers correspond to neutral hydrogen column densities of $10^{18} - 10^{20} \text{ cm}^{-2}$ (Churchill et al. 2000; Rao et al. 2006), densities that exist in collapsed objects. Blind surveys of galaxies near QSO sightlines yield Mg II absorbers a high fraction of the time (Tripp & Bowen 2005; Chen & Tinker 2008), and known Mg II absorbers are nearly always found to be associated with a galaxy with a projected separation significantly less than the virial radius of the dark matter halo around that galaxy (e.g., Bergeron 1986; Steidel 1993; Kacprzak et al. 2008). Mg II absorbers thus probe the cool gas around galaxies from which these galaxies form their stars. The redshift evolution of absorbers is thus connected both to the growth of dark matter structures and the evolution of gas accretion in dark matter halos. Connecting quasar absorbers with dark matter halos is a direct probe of the gas accretion history of such objects.

The observed statistics of Mg II absorbers are a consequence of the properties of the halos in which the gas resides. In this paper we present a model that provides a mapping between rest-frame Mg II absorption equivalent width, $W_r(2796)$ (hereafter W_r) and dark matter halo mass M_h in such a way as to match the frequency function of absorbers, their large-scale clustering bias, and the redshift evolution of their number counts.

The methods for quantifying the connection of galaxies to

dark matter halos are now well established through halo occupation models (see, e.g., Seljak 2000; Scoccimarro et al. 2001; Cooray & Sheth 2002; Berlind & Weinberg 2002 for early works and Zheng et al. 2007; van den Bosch et al. 2007; Tinker et al. 2007 for examples of more recent extensions of the analysis). In Tinker & Chen (2008) (hereafter Paper I), we presented a model of the halo occupation of cold gas that addressed the first two of these issues: the frequency and bias functions at $z = 0.6$. Our approach in Paper I was to parameterize the conditional probability of an absorber being produced by a halo of given mass $P(W_r|M_h)$ and using the statistics of dark matter halos to constrain the free parameters of $P(W_r|M_h)$ in order to match the observations. After adopting a cored isothermal density profile for the Mg II gas (a choice later supported in Chen & Tinker 2008, hereafter Paper II), the two free quantities governing $P(W_r|M_h)$ were constrained from the data: the incidence of absorption per halo $\kappa_g(M_h)$ and the absorption efficiency $A_W(M_h)$. The former encapsulates both the covering fraction of Mg II gas in the dark matter halo and the incidence of extended gaseous halos. The latter controls the mean absorption strength as a function of halo mass. Because the halo-based model parameterizes these two quantities, it makes no assumptions about the physical nature of these systems—whether they are produced from infalling or outflowing gas, or within a turbulent, static gas halo. The primary purpose of this model is to determine the distribution of halo masses probed by Mg II absorbers and the incidence required to match observations.

The difficulty in reconciling halo statistics with measured statistics of Mg II absorbers at $z = 0.6$ lies in the observed anti-correlation between W_r and the large-scale clustering bias b_W (Bouché et al. 2006; Gauthier et al. 2009; Lundgren et al. 2009). For dark matter halos, the most biased objects are the rarest and most massive. The anti-correlation between

W_r and b_W implies that the most biased absorption systems are the weakest, most frequent systems. In Paper I we concluded that the $f(W_r)$ and b_W data could only be fit by a model that contained a critical mass scale below which absorption efficiency is high, but at higher masses the absorption efficiency is significantly attenuated due to a lack of cold gas in the halo. This transition from ‘cold-mode’ gas accretion to ‘hot-mode’ accretion is motivated by results of analytic models and numerical simulations that demonstrate a critical halo mass at which shock heating becomes efficient (Birnboim & Dekel 2003; Kereš et al. 2005, 2008; Dekel & Birnboim 2006; Birnboim et al. 2007; Brooks et al. 2008). These simulations found that the transition between the cold mode and hot mode occurs between $10^{11} h^{-1} M_\odot$ and $10^{12} h^{-1} M_\odot$, precisely the location required to match the Mg II statistics. The expectations of these papers are qualitatively similar to those from two-phase gas cooling models of Mo & Miralda-Escude (1996) and Maller & Bullock (2004). In these models, in halos below $\sim 10^{11.5} h^{-1} M_\odot$ gas cooling is rapid, while at higher masses the fraction of cold gas in the halo (in the form of pressure-supported cold clouds) decreases exponentially with halo circular velocity, leaving only a small fraction of cold gas at $M_h \gtrsim 10^{13} h^{-1} M_\odot$. These observational trends may also be produced if the distribution of cold gas changes within the halo as well; the cold gas fraction may remain constant but be redistributed into a smaller cross section within dense gas clumps or be less extended in the dark matter halo. Along with a high-mass cutoff, the data also require a low-mass cutoff below $M \sim 10^{11} h^{-1} M_\odot$ due to the high overall bias of absorbers. The theoretical motivation for such a cutoff is less clear than a high-mass cutoff, and we will discuss both equally in this paper.

Paper I demonstrated that the anti-correlation between W_r and b_W is produced from residual amounts of cold gas in hot-mode halos. This small amount of cold gas can produce only low equivalent width absorption in $M_h \gtrsim 10^{13} h^{-1} M_\odot$ halos, increasing the bias of low- W_r systems. This scenario is similar to the “cold streams” seen in simulations (Kereš et al. 2005; Birnboim et al. 2007).

In Paper II we used an observational sample of galaxies in quasar fields to test the assumptions and results of Paper I: namely, that the extent of the Mg II gas radius is equal to $1/3$ the dark matter halo radius, thus scaling as $M_h^{1/3}$. Brighter galaxies occupy more massive halos, thus the implication of this assumption is that the radial extent of Mg II absorption around galaxies scales with luminosity such that

$$R_g = R_{g*} \left(\frac{L}{L_*} \right)^\alpha. \quad (1)$$

Paper I assumed that $R_{g*} \approx 80 h^{-1} \text{kpc}$ and $\alpha \approx 0.42$, values obtained from the mean halo radius of L_* galaxies derived from halo occupation analyses of galaxy clustering at multiple redshifts (ie, Tinker et al. 2007; van den Bosch et al. 2007; Zheng et al. 2007). These assumptions were in good agreement with the observational sample of Paper II: $R_{g*} = 91 h^{-1} \text{kpc}$ and $\alpha = 0.35$. Once accounting for the intrinsic scaling between galaxy luminosity and halos radius, we found the incidence of absorption to be $> 80\%$ for $L \sim L_*$ galaxies, echoing the result from Paper I that κ_g must be nearly unity at $\sim 10^{12} h^{-1} M_\odot$ to account for the frequency of absorption at $z \sim 0.6$.

In this paper, we extend the results of Papers I and II to

constrain the redshift evolution of halo occupation of the cool gas probed by Mg II systems. We present two complementary models of gas-halo evolution, demonstrating that measurements of the clustering of absorbers at multiple epochs can provide constraints on the relative contribution of each evolutionary scenario. We make predictions for the evolving connection between absorbers and dark matter halos from a single model constrained to match the same critical mass scale between cold-mode and hot-mode halos and found in Paper I and predicted by the hydrodynamic simulations listed above.

Throughout this paper we assume cosmological parameters in agreement with the results of Spergel et al. (2007): $\Omega_m = 0.25$, $\Omega_\Lambda = 0.75$, $n = 0.96$, $h = 0.7$, and $\sigma_8 = 0.8$. All units assume $H_0 = 100 h \text{ km s}^{-1} \text{ Mpc}^{-1}$. All distances are in comoving units unless otherwise stated.

2. HALO VS. ABSORBER EVOLUTION

Prochter et al. (2006a) measured the redshift evolution of absorber counts from Data Release 3 of the Sloan Digital Sky Survey. Figure 1 shows the Prochter et al. (2006a) results broken into three bins in equivalent width. They found that the number of absorbers per line of sight per unit redshift, $n(z)$, increases by nearly a factor of 3 from $0.5 < z < 1.5$ for $W_r > 1$ systems, translating to roughly a constant number of absorbers per unit comoving distance. This is the opposite to the growth of dark matter structure; as redshift increases, the amplitude of dark matter fluctuations decreases, reducing the number of dark matter halos. The thick gray curve in Figure 1a indicates $n(z)$ for dark matter halos with $M \geq 10^{11} h^{-1} M_\odot$ (roughly the mass scale for $L \sim 0.1 L_*$ galaxies), weighted by the cross section of each halo. The halo number counts decrease by more than a factor of 5 over the same redshift range as the observations. The apparent anti-theoretical evolution of halos and absorbers indicates that the gaseous content of dark matter halos must be evolving with cosmic time.

A change in the Mg II gaseous cross section physically corresponds to a change in the amount and/or distribution of cool, metal-enriched gas in the dark halo population. This could result from a change in gas accretion onto the halo or in outflows from the galaxy within the halo, as well as a redistribution of the metal-enriched cold gas within the halo. In purely geometric terms, these changes could result in an expansion or contraction of the extent of the gaseous halo per object, or it could change the total number of halos contributing to the overall cross section. Because the focus of our model is to accurately constrain the halo distribution producing the absorption, we parameterize the geometric consequences of an evolving baryonic content without making assumptions about the mechanisms. Thus we consider two modes of gas-halo evolution that can counterbalance the growth of cosmic structure. First, the cross section per halo may be changing with redshift. In this evolutionary mode, the halo mass regime in which Mg II absorption originates is constant, but the cross section per halo grows at a rate commensurate with the decreased halo abundance. We will refer to this scenario as “radius evolution”. In the second evolutionary mode, the extent of the gas halo (with respect to its dark matter halo) is constant with redshift, but the halo mass scale evolves. In Paper I we found that κ_g for halos of $M \lesssim 10^{11} h^{-1} M_\odot$ falls off steeply, thus these halos contribute little to the overall cross section at $z = 0.6$. In the cold mode/hot mode paradigm, all halo gas at this halo mass scale should be cold, thus the decreased cross section is more likely to be explained by a change in the distri-

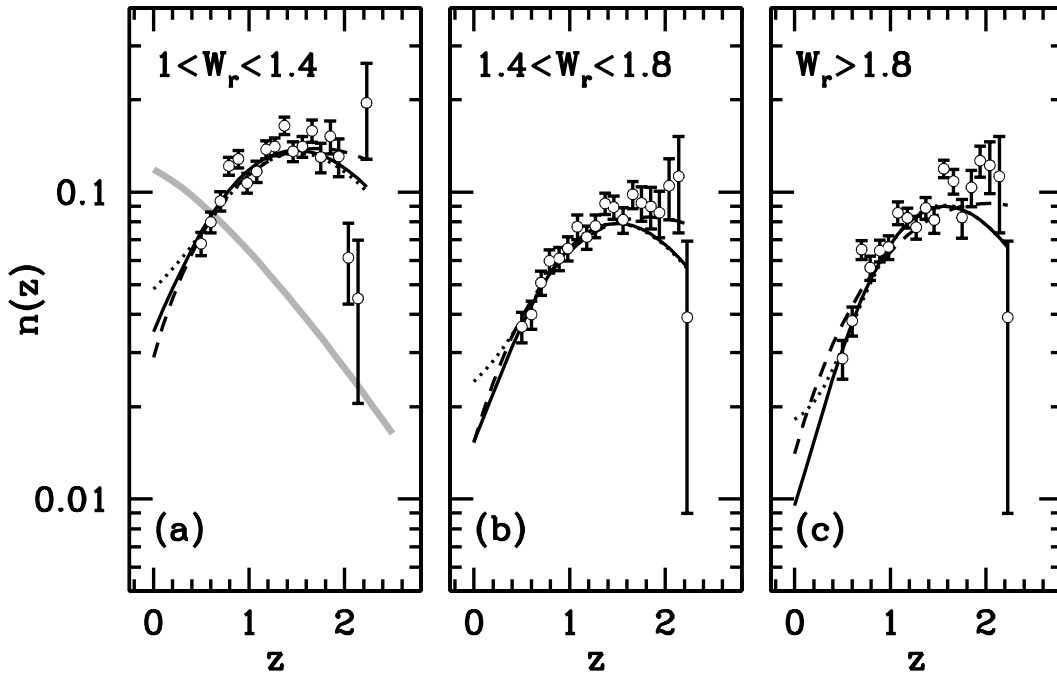


FIG. 1.— The redshift evolution of absorber counts. Points with error bars represent the measurements of Prochter et al. (2006a) broken into three bins of equivalent width. The dashed and dotted curves represent the radius and mass evolution models, respectively, described in §2. The solid curves represent the combined model, discussed in §5. The thick gray line in panel (a) shows its evolution of dark matter halo counts for $M_h > 10^{11} h^{-1} M_\odot$ multiplied by a factor of 0.01 for comparison to the data.

TABLE 1
PARAMETERS OF THE BEST-FIT MODELS

Model	A_W	α_A	\hat{R}_{sh}^0	γ_{sh}	$\log M_{\text{crit}}$	$\log \kappa_1$	$\log \kappa_2$	$\log \kappa_3$	$\log \kappa_4$	f_{cold}	β_M	β_R	χ^2
Mass Evol.	23.4	0.208	1.57	1.19	11.1	-1.60	-0.445	-0.053	-0.114	0.108	3.51	—	117.7
Radius Evol.	10.2	0.047	0.566	0.638	11.9	-2.48	-1.02	-0.001	-0.001	0.057	—	1.47	122.7
Combined	14.5	0.197	1.00	1.00	11.5	-2.00	-0.520	-0.130	-0.5477	0.114	2.52	0.41	122.4

bution of cold gas or metal content than a change in the temperature structure of the gas. We discuss a possible physical interpretation of the behavior at low mass in §6.2. If this lower mass limit decreases with increasing redshift, it would compensate for the lower overall amplitude of the mass function at high z . We will refer to this scenario as “mass evolution”.¹

Absorber number counts, either in the form of $n(z)$ or the frequency function $f(W_r)$, cannot distinguish between these two scenarios. However, measurements of the large-scale bias factor b_W can break the degeneracy and discriminate between radius and mass evolution. These two evolutionary processes are complementary but not mutually exclusive; the truth may

¹ There is also the possibility that absorption efficiency, A_W , changes with redshift at fixed halo mass. This is effectively similar to radius evolution; increasing the strength of absorption expands the radius at which a given W_r occurs, even though the extent of the gas radius is fixed. However, without any change in the gas radius relative to R_{halo} , this form of evolution cannot match the observations; the increase in the cross section at high W_r comes at the expense of cross section at lower W_r . The total number of absorbers integrated over all equivalent width cannot change. Because radius evolution entails an increase in the cross section per halo at fixed W_r , we concentrate on the first two scenarios.

lie somewhere in between. In a third model, we constrain the relative contributions of mass and radius evolution with a model constrained to match the expected transition mass scale between cold mode and hot mode accretion found in Paper I. We will discuss this “combined evolution” model in detail in §5.

One point to stress is that dark matter halos have comoving radii that are *constant* at fixed halo mass. The transition regions between virialization, infall, and Hubble flow are determined by the background matter density, which is constant in comoving units as well. In physical units, dark matter halos “shrink” as redshift increases, but their density relative to the background is constant. This will become important when discussing $\kappa_g(M, z)$ for low-mass halos.

3. METHODS

3.1. The Halo Occupation Model for Cold Gas

To construct the gaseous halo, we follow the outline in Paper I with minor modifications that we note below. First we choose the density profile of the cool, clumpy gas that forms

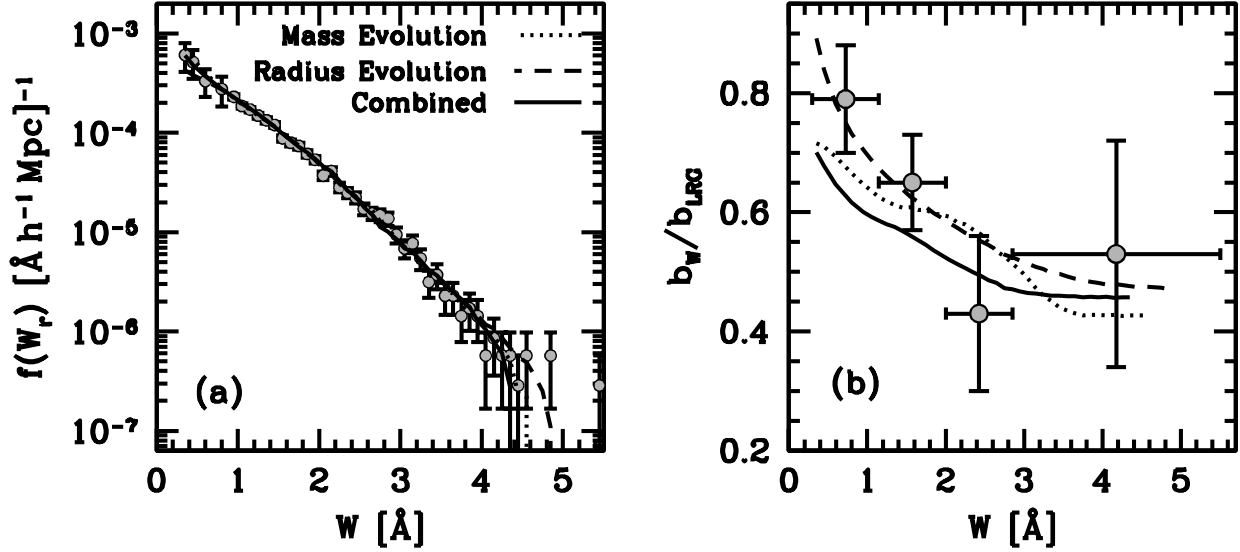


FIG. 2.— Panel (a): Comparison between $f(W_r)$ of the models fits and the data. Panel (b): Comparison between the b_W/b_{LRG} at $z = 0.6$ from the models and the Bouché et al. (2006) data. The models cannot be distinguished by frequency data and by bias data at only one redshift.

part of the gaseous halo responsible for Mg II absorption. We assume this profile to be a cored isothermal model of the form

$$\rho_{\text{gas}}(r) \propto (r^2 + a_h^2)^{-1}. \quad (2)$$

The absorption equivalent width is proportional to the projected density at a given impact parameter, ρ_b . This is consistent with observations that demonstrate that Mg II absorbers seen in low-resolution spectra are broken into discrete components—cold clumps or clouds—when observed in high resolution. The total W_r is linearly proportional to the number of components. This leads to a relationship between impact parameter and W_r of

$$W_r(\rho_b) \propto \frac{1}{\sqrt{\rho_b^2/a_h^2 + 1}} \arctan \sqrt{\frac{R_g^2 - \rho_b^2}{\rho_b^2 + a_h^2}}, \quad (3)$$

where R_g is the extent of the cool-gas halo. A relationship of this form is in good agreement with the results of Paper II. The results of Paper II also indicate that the extent of the Mg II gaseous halo is $R_g \approx 0.4R_{200}$ at $z = 0.6$ and $a_h/R_g \approx 0.2$. We define the dark matter halo as having a mean interior density 200 times the cosmic mean density, thus

$$R_\Delta = \left(\frac{3M_h}{4\pi\bar{\rho}_m\Delta} \right)^{1/3}, \quad (4)$$

where $\bar{\rho}_m = \rho_{\text{crit}}\Omega_m$ and $\Delta = 200$. Recall that equation (4) implies that the *comoving* halo radius is the *same* at all redshifts for halos of the same mass.

We normalize the $W_r(\rho_b, M_h)$ relation (Eq. [3]) by the equivalent width obtained by a sightline that passes through the center of the halo,

$$W_r(0|M_h) = A_W(M_h)M_{12}^{1/3}, \quad (5)$$

where M_{12} is the halo mass in units of $10^{12} h^{-1} M_\odot$. The function $A_W(M_h)$ encapsulates physical properties of the gas halo, including the fraction of Mg II gas and the properties of the

cold clouds or clumps within the halo. If the Mg II gas fraction were fixed, more massive halos would contain more Mg II gas and have a larger path length at $\rho_b = 0$, thus the natural scaling of W_r is to increase as $M_h^{1/3}$. The function $A_W(M_h)$ represents deviations from this natural scaling. Some dispersion about $W_r(0|M_h)$ is indicated from the results of Paper II, but this affects $W_r(\rho_b)$ at small impact parameters where the cross section is too small to make a significant impact on the calculations. The dependence of W_r on ρ_b and M_h is then

$$W_r(\rho_b, M_h) = \frac{1}{\sqrt{\rho_b^2/a_h^2 + 1}} \arctan \sqrt{\frac{R_g^2 - \rho_b^2}{\rho_b^2 + a_h^2}} \left[\frac{W_r(0|M_h)}{\arctan(R_g/a_h)} \right], \quad (6)$$

where the factor of $1/\arctan(R_g/a_h)$ is to normalize the expression, due to the fact that equation (3) does not asymptote to unity at $\rho_b = 0$.

Above a certain mass scale, shock heating eliminates the majority of cold halo gas, attenuating the absorption efficiency of the halo. We introduce a free parameter f_{cold} to set the fraction of remaining cold gas once the halo becomes fully shock-heated. The resulting $W(\rho_b|M_h)$ in the hot mode is simply equation (6) multiplied by f_{cold} . In between the cold and hot modes, gas heating occurs as an inside-out process, resulting in a shock-heated core of gas with core radius that increases with halo mass (see, eg, Dekel & Birnboim 2006). We parameterize the dependence of the shock radius with mass as

$$\frac{R_{\text{sh}}}{R_g} = \hat{R}_{\text{sh}}^0 + \gamma_{\text{sh}} \log M_{12}, \quad (7)$$

and restrict R_{sh}/R_g to be no smaller than 0 and no larger than 1. Inside R_{sh} , the absorption efficiency is reduced by $1 - f_{\text{cold}}$. The form of equation (7) is motivated by the simulation results of Kereš et al. (2005), in which the fraction of cold accreted gas decreases linearly with $\log M_h$ through the transition region. We will refer to the “transition mass” M_{crit} as the mass at which $R_{\text{sh}}/R_g = 0.5$.

It is not necessary for a sightline that passes through a halo to produce any absorption; the clumpy nature of the cold gas may create a covering fraction of less than unity. Alternately, only a fraction of halos may contain extended Mg II gas halos. We define the product of the covering fraction and incidence as $\kappa_g(M_h)$, the probability that a halo produces absorption if intersected along the line of sight. We will define the functional form of $\kappa_g(M_h)$ in the following section. See Paper I for full details on the calculation of $P(W_r, M_h)$.

3.2. Parameterizing the dependence of $P(W_r)$ on halo mass and redshift

In Paper I we set A_W to be a constant with halo mass. This assumption was influenced more by statistics than theory; although there is no reason to expect that absorption efficiency should remain constant with halo mass, the data used were not sufficient to constrain a mass-dependent A_W . The addition of $n(z)$ ameliorates this problem. We add an additional degree of freedom by allowing the absorption efficiency to vary in the cold mode:

$$A_W(M_h) = \begin{cases} A_0 M_{12}^{\alpha_A} & \text{if } M_h < M_{\text{crit}} \\ A_0 (M_{\text{crit}}/10^{12})^{\alpha_A} & \text{if } M_h \geq M_{\text{crit}}. \end{cases} \quad (8)$$

We will discuss the effect of this addition in more detail in §5.2. As in Paper I, we model the mass dependence of κ_g non-parametrically; we set the values of κ_g at four masses and spline interpolate between these masses: $\log M_i = 10.0, 11.33, 12.66, \text{ and } 14.0$, and refer to the values of κ_g at these masses as κ_{1-4} .

To parameterize the mass evolution mode we adjust κ_g as a function of redshift. In Paper I we found that $\kappa_g \approx 1$ at $M > 10^{12} h^{-1} M_\odot$, and it rapidly falls at lower masses. Thus, instead of altering the values of κ_{1-4} , we assume that the *shape* of $\kappa_g(M_h)$ is fixed at all redshifts, but the *mass scale* evolves with time. In other words,

$$M_i(z) = M_{i,0} \exp[-\beta_M(z-z_0)], \quad (9)$$

where $i = 1-4$, and $M_{i,0}$ is the value at $z_0 = 0.6$ listed in the paragraph above. We choose an exponential form for equation (9) because it describes the growth rate of individual halos well (Wechsler et al. 2002; van den Bosch 2002). Cluster-sized halos have high growth rates, while halos less massive than the Milky Way have little evolution between redshifts 1 and 0. With equation (9), a comparison can be made between the growth rate required to match $n(z)$ and that of halos of multiple mass scales.

In pure radius evolution, the values of M_i are held constant at all z , but the gas radius evolves as

$$R_g(M_h, z) = R_{200}(M_h) \times 0.4 \left(\frac{1+z}{1+z_0} \right)^{\beta_R}. \quad (10)$$

Equation (10) implies that the gas radius can evolve with respect to the virial radius of the dark matter. A value of $\beta_R = 1$ is equal to the gas radius being fixed in physical units, while a value of $\beta_R = 0$ means the gas halo is fixed in comoving units, i.e., a fixed fraction of the dark matter halo radius.

In both models we have ten free parameters: in both models there are four that govern the covering fraction ($M_1 - M_4$), two that control the cold-hot transition (R_{sh}^0 and γ_{sh} from equation 7), one for the cold fraction within the hot mode (f_{cold}), and two that control the absorption efficiency parameter $A_W(M)$

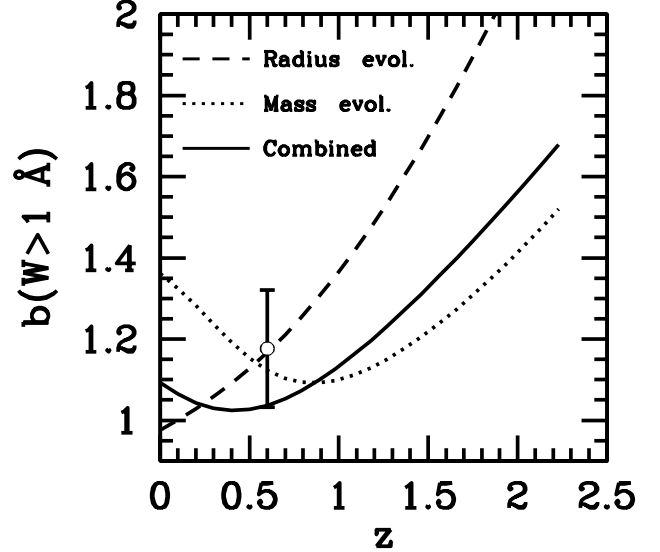


FIG. 3.— Predictions for the bias of $W_r > 1 \text{ \AA}$ absorbers for each of the three evolutionary models. The data point at $z = 0.6$ is the overall bias of absorbers from Bouché et al. (2006). The bias curves represent the absolute bias with respect to the underlying dark matter distribution.

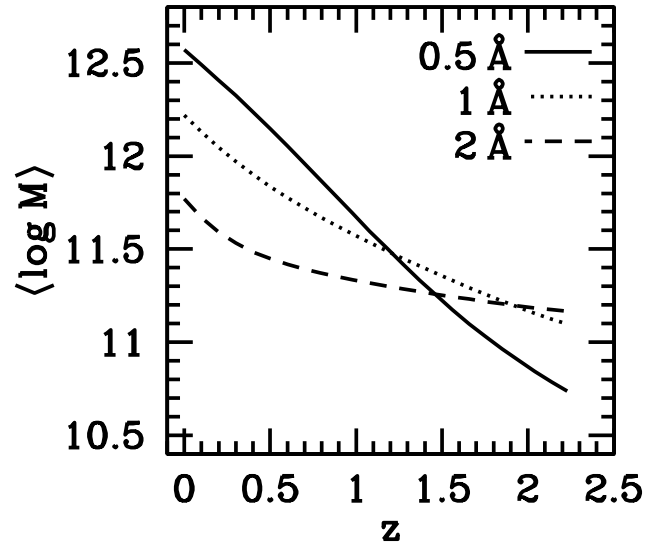


FIG. 4.— The mean logarithmic halo mass for three different values of W_r . $\langle \log M \rangle$ evolves strongly with redshift for weak absorbers but is nearly flat for strong absorbers. At $z < 1$, this produces the $b_W - W_r$ anti-correlation. At $z \sim 1.3$, W_r is roughly independent of redshift. At higher z , W_r and b_W are positively correlated.

(A_0 and α_A from equation 8). In each model there is one parameter to govern redshift evolution (β_M and β_R from equations 9 and 10, respectively). This is two more parameters than in Paper I, but we have added 57 data points for $n(z)$ in three W_r ranges, for a total of 104 data points.

3.3. Calculating Observables with the Model

Once $P(W_r|M_h, z)$ is known, the redshift evolution of absorber counts is obtained by integrating this probability dis-

tribution function (PDF) over the cross section-weighted halo mass function, i.e.,

$$n(z) = \frac{c}{H_0} [\Omega_m(1+z)^3 + \Omega_\Lambda]^{-1/2} \int_{W_{\min}}^{W_{\max}} dW_r \times \quad (11)$$

$$\int dM_h \left(\frac{dn}{dM_h} \right)_z \sigma_g(M_h, z) P(W_r | M_h, z),$$

where dn/dM_h is the halo mass function, for which we use the numerical results of Tinker et al. (2008). The subscript z on dn/dM_h indicates that the mass function is calculated at that specific redshift. The prefactor on the right hand side converts the linear density of absorbers from number per unit comoving distance to number per unit redshift. We use the data from Prochter et al. (2006a) for $n(z)$ in three bins in equivalent width: $W_r = [1.0, 1.4] \text{ \AA}$, $W_r = [1.4, 1.8] \text{ \AA}$, and $W_r > 1.8 \text{ \AA}$. To estimate the errors on the data we add the Poisson fluctuations in quadrature with a 5% ‘systematic’ error. Prochter et al. (2006a) do not estimate the cosmic variance of their measurements, and it can be seen in Figure 1 that the point-to-point variations in $n(z)$ can be significantly larger than the error bars we have estimated, suggesting that the true errors are underestimated.

The frequency function of absorbers is obtained by integrating over both mass and redshift at a given W_r :

$$f(W_r) = \frac{1}{g_{\text{tot}}} \int dz g(z) \int dM_h \left(\frac{dn}{dM_h} \right)_z \sigma_g(M_h, z) P(W_r | M_h, z), \quad (12)$$

where $\sigma_g = \pi R_g^2$,

$$g_{\text{tot}} = \int dz g(z), \quad (13)$$

and $g(z)$ is the survey completeness function at each redshift (from Prochter et al. 2006a). As in Paper I, we construct the $f(W_r)$ data from a combination of Prochter et al. (2006a) for $W_r > 1 \text{ \AA}$, and Steidel & Sargent (1992) for $0.3 \text{ \AA} < W_r < 1.0 \text{ \AA}$, where we have adjusted the normalization of the Steidel & Sargent (1992) data to the level of the Prochter et al. (2006a) results at $W_r = 1 \text{ \AA}^2$. As with $n(z)$, we estimate the errors through a quadrature addition of Poisson errors and a 5% systematic error bar.

The bias of absorbers is calculated in manner similar to $f(W_r)$, but now each halo is weighted by its large-scale bias $b(M_h, z)$ (using the bias formula of Tinker et al. 2005).

$$b_W(z) = \frac{1}{f(W_r, z)} \int dM \left(\frac{dn}{dM} \right)_z \sigma_g(M, z) b_h(M, z) P(W_r | M, z). \quad (14)$$

When comparing to the data we set $z = z_0 = 0.6$. Bouché et al. (2006) measure the bias of Mg II absorbers by cross-correlating absorbers with luminous red galaxies (LRGs) from the Sloan Digital Sky Survey photometric catalog. To compare the models to the data, we calculate the absolute bias of absorbers from equation (14) and divide the calculation by

² Due to an error in the normalization of the Prochter et al. (2006a) data, we have increased the amplitude of $f(W_r)$ and $n(z)$ by 30% (J. X. Prochaska, private communication). This adjustment brings the Prochter et al. (2006a) data into agreement with the $n(z)$ fitting function given in Prochter et al. (2006b), which is based on more recent results.

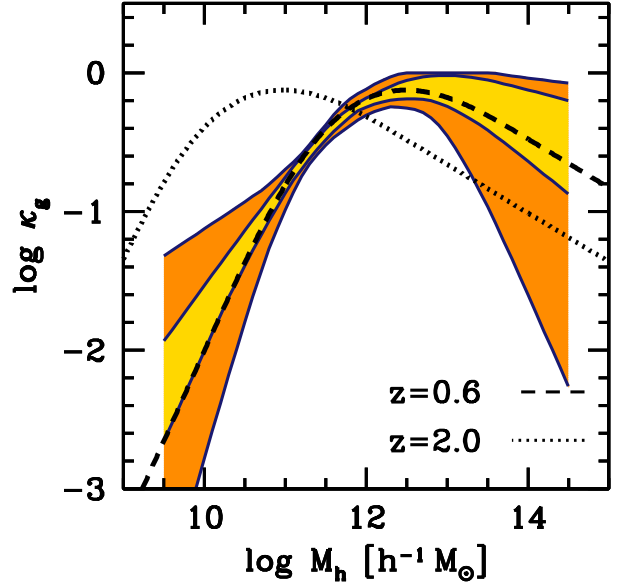


FIG. 5.— Constraints on the covering factor within R_g from the combined model. Inner and outer contours represent models with $\Delta\chi^2 < 1$ and 4 with respect to the best fit model, respectively. The dashed curve is the best-fit model at $z = 0.6$, while the dotted curve represents $\kappa_g(M)$ at $z = 2.0$. At $z = 2$, the decrease in κ_g above $10^{12} h^{-1} M_\odot$, has little effect on the Mg II statistics because the abundance of hot-mode halos is significantly attenuated at this and higher redshifts.

the bias of LRGs at $z = 0.6$, $b_{LRG} = 1.81$ (White et al. 2007). The bias data are in four bins of W_r : $[0.3, 1.15] \text{ \AA}$, $[1.15, 2.0] \text{ \AA}$, $[2.0, 2.85] \text{ \AA}$, and $[2.85, 4.0] \text{ \AA}$. When comparing models to bias data, we take the number-weighted average bias over the given range in W_r . See Paper I for further details.

When calculating observables, we truncate the integrals over mass at $M_h = 10^9 h^{-1} M_\odot$. We find that extending this limit to lower masses produces negligible differences in the model predictions, even at high redshift. We find the best-fit models by minimizing the total χ^2 from the sum of the χ^2 values from $f(W_r)$, $n(z)$, and b_W . We use the Monte Carlo Markov Chain (MCMC; see, e.g., Dunkley et al. 2005) method to minimize χ^2 and quantify the constraints on individual parameters. Results of the fitting are listed in Table 1.

4. RESULTS

Figure 1 presents the best-fit models for both the mass evolution model and the radius evolution model (we will discuss the combined model subsequently). Both these models produce statistically good fits, with $\chi^2/\nu = 1.30$ for radius evolution and $\chi^2/\nu = 1.25$ for mass evolution, with the caveat that the error bars are only estimates, and no covariance between data points is accounted for. Figure 2 compares the model fits to the $f(W_r)$ and bias data. The results for $f(W_r)$ from each model are nearly indistinguishable, producing the observed exponential distribution of absorbers. In our model, the exponential distribution of absorber equivalent widths is produced primarily from the cutoff in absorber efficiency in the hot mode. At $W_r < 1 \text{ \AA}$, there is evidence that $f(W_r)$ becomes a power law (Steidel & Sargent 1992; Nestor et al. 2005). Above $W_r = 2 \text{ \AA}$, most all absorbers are produced in halos in the transition stage, $M_h \approx 10^{11.5} h^{-1} M_\odot$. Without a high-mass cutoff, $f(W_r)$ is a power-law that overproduces the

abundance of high- W_r systems. Below 1 \AA , the abundance of absorbers is not attenuated by the hot mode, thus producing a steeper $f(W_r)$. This is not a unique solution to the problem; it is straightforward to construct a mass-dependent covering factor function that maps the M_h^{-2} halo mass function to the $\exp(-W_r)$. However, without the high-mass cutoff one cannot fit both the $f(W_r)$ and clustering data at the same time. Both evolution scenarios produce excellent fits to b_W at $z = 0.6$, yielding a strong anti-correlation with W_r , as shown in Figure 2. The amplitude of b_W at z_0 is somewhat higher in the radius evolution model due to the lower value of R_{sh}^0 , which controls the transition mass M_{crit} . The higher mass scale for absorbers in the radius evolution model increases the bias at all W_r .

As expected, both models produce nearly identical fits to $n(z)$; the number counts alone cannot distinguish between these models. To match $n(z)$ in the radius evolution model, the gas radius must increase relative to R_{200} as $(1+z)^{1.47 \pm 0.05}$. Prochter et al. (2006a) find that $n(z)$ increases roughly as $(1+z)^{1.4}$. Because the gas cross section scales as R_g^2 , the redshift evolution of the cross section (at fixed halo mass) is much larger than the increase in the number counts themselves. However, this is counterbalanced by the reduced frequency of dark matter halos at higher redshifts, producing an increase in absorber counts consistent with the data. However, in order to match the number counts, the gas radius must *expand in physical units* to keep the total gas cross section constant because the number of halos is decreasing with look-back time. At this level of evolution, the gas radius is *twice* the virial radius of the dark matter halo at $z = 2$, with nearly unit covering factor and incidence.

For the mass evolution model, the growth rate of the κ_g mass scale is $\beta_M = 3.5 \pm 0.2$. This evolution rate is much larger than that found in dark matter halos; from Wechsler et al. (2002), halos with $z = 0$ masses near $10^{12} h^{-1} M_\odot$ have growth rates of ~ 0.6 , while $z = 0$ clusters have growth rates of ~ 1.3 . This best-fit value of β_M is nearly the same as the evolution rate of the non-linear mass scale, which approximately sets the average mass scale of structures that are collapsing at a given epoch. The non-linear mass scale roughly indicates the halo mass above which the halo mass function experiences a Gaussian cutoff. The similarity between the best-fit β_M and the non-linear mass scale is not surprising, given that the model is preserving the number of absorbers in a cosmology in which the exponential cutoff in the mass function evolves. Adding lower mass halos to the total gas cross section at the same rate counterbalances the effect of the decreasing amplitude of fluctuations at higher z .

One avenue for discriminating between these two models lies in their constraints on the transition between cold and hot modes. In order to fit the data, the two evolutionary models required the hot/cold transition scale be substantially different. For radius evolution, $M_{\text{crit}} = 10^{11.9} h^{-1} M_\odot$, while mass evolution produces $M_{\text{crit}} = 10^{11.1} h^{-1} M_\odot$. Hydrodynamic simulations yield results in between these two values.

An empirical approach for discriminating between these models is the evolution of their clustering. At different redshifts the two evolutionary scenarios place the cold gas in different halos. Thus, they make distinct predictions for the evolution of absorber bias. In Figure 3, we show b_W for absorbers with $W_r > 1 \text{ \AA}$ as a function of redshift for both models. The data point is taken from Bouché et al. (2006), and it has been multiplied by b_{LRG} to recover the absolute bias of

the absorbers. In the radius evolution model $b_W(z)$ increases rapidly. The mean mass scale of absorbers in this model is nearly constant with redshift, but halos at fixed mass correspond to increasingly rare objects at higher redshift, resulting in increased bias. In the mass evolution model, the mass scale decreases such that the b_W at $z = 1.5$ is the same as it is at $z = 0.6$. The large difference between the predictions of these two models demonstrates the potential of discriminating between these two types of evolution based solely on their clustering, either at high redshift or at $z \sim 0$. Bias values in between these two extremes would represent a combination of the two evolutionary modes. The bias curves also diverge at low redshifts. The difference between the models at $z = 0.1$ is not much larger than the $z = 0.6$ error bar, so bias measurements at lower redshift require more precise $z = 0.6$ data to constrain models. However, ongoing spectroscopic surveys should significantly enhance current $z = 0.6$ measurements³.

5. PREDICTIONS OF A COMBINED MODEL

Numerical results and analytical calculations place M_{crit} at $\sim 10^{11.5}$.⁴ These results are in good agreement with the constraint on M_{crit} at $z = 0.6$ from Paper I. Thus, in our “combined” model mentioned in §2, we fix the hot/cold transition to be $M_{\text{crit}} = 10^{11.5} h^{-1} M_\odot$, with a transition width of 1 decade in mass. With these parameters fixed, we are able to leave both evolutionary modes as free parameters and constrain their relative contribution to gas halo evolution. With the transition parameters fixed to those expected from simulations, both evolutionary models contribute, but mass evolution dominates the overall evolution of gaseous halos ($\beta_M = 2.52 \pm 0.24$, $\beta_R = 0.41 \pm 0.11$). The full parameter set is given in Table 1.

It is important to note that there are many ways to parameterize this problem, and the data do not currently exist that afford us the freedom of making predictions without the use of priors on some of our parameters. Our choices are driven by the theoretical results discussed above. But as we demonstrated in §4, different choices for these parameters result in a different halo occupation of absorbers and result in different predictions for the clustering of absorbers and their connection to galaxies of different luminosities. These are predictions that further observational results will be able to test.

5.1. The Bias of Absorbers

The evolution of absorber bias is shown with the solid curve in Figure 3. Because mass evolution dominates this model, the slope of bias with redshift is slightly steeper than from mass evolution alone. Figure 4 shows the mean logarithmic mass of absorbers as a function of redshift. For weak absorbers, $W_r = 1 \text{ \AA}$, $\langle \log M \rangle$ is a strongly decreasing function of z . Strong absorbers, however, predominantly arise at $M_h \sim M_{\text{crit}}$ regardless of redshift; in the cold mode, $W_r \sim A_w M_h^{1/3}$, thus the strongest absorbers arise in the most massive halos before the transition to shock heating. For $W_r \sim 2 \text{ \AA}$ absorbers, $\langle \log M \rangle \approx 11.3$ and it is nearly independent of redshift at $z > 0.5$.

At $z = 0.6$, W_r and $\langle \log M \rangle$ are anti-correlated, yielding the b_W - W_r anti-correlation measured. From Figure 4 it is apparent

³ Baryon Oscillation Spectroscopic Survey, <http://cosmology.lbl.gov/BOSS/>

⁴ We note that the canonical value of $10^{12} h^{-1} M_\odot$ obtained by Dekel & Birnboim (2006) specifies the mass at which the entire halo has been shock-heated, rather than the mass at which half the halo is within the shock radius, as we have defined it.

that the anti-correlation goes away at $z = 1.3$, and at $z > 2$ W_r and $\langle \log M \rangle$ (and also b_W) are positively correlated. At $z > 2$, the abundance of halos above M_{crit} is negligible, thus they no longer contribute to the clustering statistics of absorbers. The predictions for pure mass evolution are similar to those in Figure 4, but for pure radius evolution the predictions are markedly different. In radius evolution, the shape of the b_W - W_r anti-correlation is preserved at all redshifts. Thus, another method for discriminating between the different evolutionary modes is bias as a function of W_r at high redshift.

5.2. Incidence and Covering Factor

Figure 5 shows the constraints on the covering fraction/incidence rate of Mg II absorbers as a function of host-halo mass, κ_g . At $z = 0.6$, halos above $\sim 10^{12} h^{-1} M_\odot$ are consistent with covering factor near unity. Below this mass, the covering factor decreases roughly linearly with halo mass. The softer cutoff at low mass is somewhat different from the constraints on $\kappa_g(M_h)$ in Paper I but are consistent with the observational results of Paper II. In Paper I, κ_g for $M < 10^{11.5} h^{-1} M_\odot$ decreased rapidly, becoming essentially zero at $\sim 10^{11} h^{-1} M_\odot$. This result was driven in part by the parameterization used in Paper I, in which A_W was set to be a constant for halos in the cold mode. Here we allow A_W to vary as a power law, and in the best-fit model $A_W \sim M^{0.2}$. Thus lower mass halos have somewhat lower absorptions efficiency and may have a non-zero covering fraction without overproducing the frequency of absorbers at low- W_r .

In the hot mode, $\kappa_g \gtrsim 0.4$ at $M_h \gtrsim 10^{13} h^{-1} M_\odot$, the constraints are poor on the covering fraction, although the $1\text{-}\sigma$ lower limit is $\kappa_g \approx 10\%$. The bias data drives the constraints toward higher κ_g in this mass range; the models that reproduce the clustering anti-correlation all have $\kappa_g \gtrsim 0.4$. To match the strong clustering of $W_r \sim 1 \text{ \AA}$ absorbers, as well as the high overall clustering of absorbers, a significant fraction of systems must be produced in massive halos. However, the current level of precision on the bias data are not sufficient to place tight constraints on κ_g in the hot mode. A high incidence of absorption at this mass scale may seem difficult to reconcile with the fact that the cold fraction has been reduced by $\sim 90\%$ in our model, but the model used here may be overly simplistic. In multiphase models of gaseous halos (ie, Mo & Miralda-Escude 1996; Maller & Bullock 2004), cold gas in hot halos extends out to the virial radius, either in the form of condensed clouds or cold streams. Thus, it is possible to match the data with a much lower κ_g in the hot mode but now with $R_g \approx R_{200}$. The model predictions would be nearly identical for the current data, but the LRG-Mg II cross-correlation function would be markedly different at $r \lesssim 1 h^{-1} \text{ Mpc}$ scales. More study of the incidence and radial extent of cold gas around clusters or LRGs is required to constrain the cold gas around massive objects.

6. DISCUSSION

We have presented a model that connects Mg II absorbers to dark matter halos in order to reproduce their observed statistical properties; their clustering bias at $z = 0.6$, their frequency function, and their redshift evolution. In a model in which the transition between cold-gas halos and hot-gas halos is fixed to be $10^{11.5} h^{-1} M_\odot$, we find that the mass scale of absorbers must significantly decrease with increasing redshift in order to match the data. Although the mass scale of strong absorbers varies little with redshift, the overall mass scale of absorbers

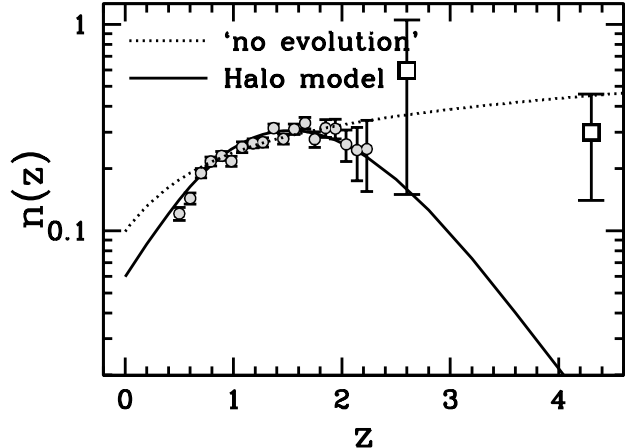


FIG. 6.— $n(z)$ for the combined evolution model, extrapolated to $z \gtrsim 4$. The circles are the Prochter et al. (2006a) data for $W_r > 1 \text{ \AA}$ ($z = 2.6$) and $W_r > 1.5 \text{ \AA}$ ($z = 4.3$). The squares are the results of Jiang et al. (2007). The dotted line is the ‘no evolution’ model, in which the number of absorbers per comoving unit distance is constant.

is maximal at $z = 0$. This upsizing is in stark contrast to the ‘downsizing’ trend in the star formation of galaxies, in which the most massive systems form their stars early and the halo mass scale at which most the star formation is occurring increases with redshift. This model makes testable predictions of the clustering of absorbers at $1 < z < 2$ and at $z \sim 0.1$.

6.1. The evolution of absorber number counts

The hot/cold transition is important in determining the slope of $n(z)$ and how that slope depends on W_r . Nestor et al. (2005) find that the slope of $n(z)$ depends strongly on equivalent width; for $W_r \sim 0.3 \text{ \AA}$, $n(z)$ is nearly constant, and the slope monotonically increases with absorption strength. The hot/cold transition, combined with the mass evolution scenario, offers a succinct explanation of this effect. Strong absorbers predominantly exist in the cold mode, thus their frequency is enhanced as the fraction of absorbers contributed by $10^{11}\text{-}10^{12} h^{-1} M_\odot$ halos increases from $z = 0.5$ to 1.5 . Weak absorbers are produced in *both* hot and cold halos, so the fraction of halos in the hot mode has less relevance. The frequency of $0.3 \leq W_r \leq 1 \text{ \AA}$ absorbers in our combined model is nearly independent of redshift, in agreement with the Nestor et al. (2005) measurements. For pure radius evolution, the shape of $n(z)$ is independent of W_r , lending further support to mass evolution as the dominant scenario.

Although the Prochter et al. (2006a) $n(z)$ data only extend to $z \sim 2.2$, it is interesting to extrapolate the models to higher redshifts. Figure 6 shows the prediction for the combined model at $z > 2$. The reduced abundance of $M \gtrsim 10^{11} h^{-1} M_\odot$ dark matter halos at high redshift eventually wins out over either mass or radius evolution; the model peaks at $z \sim 1.5$, then turn over and decreases monotonically at higher redshift. Lower-mass halos, $M \lesssim 10^{9-10} h^{-1} M_\odot$, still contain significant total cross section, but in our model the absorption efficiency of these halos is too low to produce a large cross section at $W_r \geq 1 \text{ \AA}$. The results from the mass- and radius-evolution models are quantitatively similar. The dotted curve in Figure 6 is commonly referred to as a model with

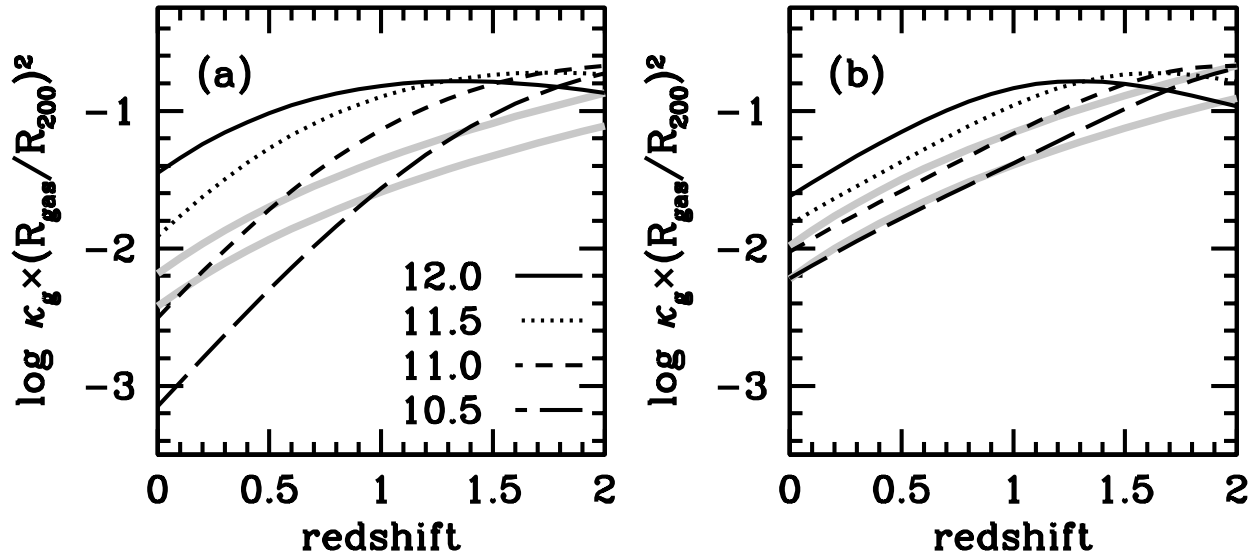


FIG. 7.— Panel (a): Redshift evolution of the total gas cross section, $\kappa_{\text{tot}} = \kappa_g (R_g/R_{200})^2$, for the best-fit combined model. The black curves represent different halo masses. The key indicated $\log M$ for each line type. The two gray curves are the toy model results, discussed in §6.2, for $\log M = 11.0$ and 10.5 (upper and lower curves, respectively). Panel (b): Same as panel a, but results are shown for the 2σ upper limit on κ_1 shown in Figure 5. Gray curves have been shifted up to compare with the halo model results.

‘no evolution’, meaning that the comoving number density of Mg II-absorbing objects is constant and that the gas cross section per object is constant in physical units. For this model, $n(z) \propto (1+z)^2 [\Omega_m(1+z)^3 + \Omega_\Lambda]^{-1/2}$. Jiang et al. (2007) have an estimate of $n(z)$ at $z = 2.6$ ($W_r > 1$) and $z = 4.3$ ($W_r > 1.5$) from a sample of six $z \sim 6$ quasars with a total redshift pathlength of $\Delta z = 0.4$. These data are preliminary; the mean number density of Mg II absorbers may change when surveys of a larger sample of QSO sightlines become available. The current data are consistent with the no-evolution model. But from Figure 6 it is clear that the no-evolution model corresponds to significant evolution with respect to the underlying halo population, both in terms of the typical halo mass and the size of the gas halo with respect to the dark matter halo. When extrapolating the halo model, the predictions are an order of magnitude below the measurements at $z = 4.3$. Removing the critical mass scale and allowing all halos to have high absorption efficiency at this redshift (as found in the analytic model of Dekel & Birnboim 2006 and the hydrodynamic simulations of Kereš et al. 2008) will not alleviate this discrepancy due to the paucity of halos above M_{crit} at this epoch.

There are two major possibilities for resolving this discrepancy; the Mg II cross-section around galaxy-type dark matter halos increases significantly beyond their virial radius, or low-mass (sometimes called ‘minihalos’) have enhanced absorption efficiency at high redshift. The former scenario could be the result of star formation in typical high-redshift galaxies, where metal-enriched gas is efficiently dispersed into the IGM to increase the cross-section of absorbing gas. The latter scenario is the proposal of Abel & Mo (1998) to explain the high frequency of Lyman-limit systems at $z > 2$. Star formation in these halos is not possible after reionization, but before that time it may be possible to form small amounts of stars and enrich the minihalos. Further data on the equivalent width distribution and absorber-galaxy pairs will be able to discriminate between these two models.

6.2. Evolution of absorbers in the cold mode

Our combined model predicts that the overall halo mass scale of Mg II absorbers reduces as redshift increases. This is caused both by the loss of massive halos as redshift increases and the increased gaseous cross section of low-mass halos in the cold mode. The rate of change of the halo mass scale for low- W_r systems is significantly faster than the growth rate of low-mass halos themselves; i.e., a $10^{11} h^{-1} M_\odot$ halo at $z = 1.5$ that produces an absorber is much less likely to produce an absorber when that halo evolves to $z = 0$ even though that halo is, on average, twice as massive.

Figure 7a shows the evolution in the mean covering fraction within halos relative to the total halo cross section, $\kappa_{\text{tot}} = \kappa_g \times (R_g/R_{200})^2$, for the combined model. At $10^{12} h^{-1} M_\odot$, this quantity does not change much with lookback time, but at lower masses the cross section at $z = 0$ is below 1% and the evolution with redshift is steep.

We can try to understand the mass and redshift trends seen in Figure 7 through a simple picture of gas accretion. The evolution of κ_g occurs in the cold mode—halos less massive than $M_h \sim 10^{11.5} h^{-1} M_\odot$. At all mass scales, the accretion of baryonic matter is expected to increase with redshift. A convenient fitting formula is

$$\dot{M}_g \approx 6.6 M_{12}^{1.15} (1+z)^{2.25} \quad (15)$$

(Dekel et al. 2008). Since there is no hot gas halo at these masses, and all gas is accreted cold, the infalling gas will simply fall to the center of the halo. We assume that it takes a free-fall time, t_{ff} , for the gas to reach the galaxy at the center of the halo—although the gas is accreted with non-zero velocity, it will also have angular momentum that must be shed before it can reach the galaxy. The important assumption is that the infall time is related to the dynamical time of the halo. The total amount of gas in a cold-mode halo is $M_g = t_{\text{ff}} \dot{M}_g$. Using

$$\begin{aligned}
t_{ff} &\approx 0.5(G\bar{\rho}_h)^{-1/2} \\
&\approx 1.4(1+z)^{-3/2} \text{Gyr}, \quad (16)
\end{aligned}$$

the total halo gas scales as $M_g \sim (1+z)^{0.75} M_h^{1.15}$. The free fall time does not depend on halo mass because all halos have the same mean density of 200 times the background, which scales as $(1+z)^3$. We are less interested in the absolute scaling of the covering factor in this toy model than the scaling with mass and redshift, so we can normalize this relation to give the proper covering fraction of $10^{11} h^{-1} M_\odot$ halos at $z = 0.5$, $\kappa_{\text{tot}} = 0.02$. Provided that the mean properties of the clumps—their sizes and densities—stay relatively constant, the covering factor of the accreted gas should scale with the amount of material and the volume throughout which they are distributed.

Not only does the gas accretion rate increase with redshift, but the physical volume in which they are spread is decreasing—recall that halos at fixed mass have constant comoving radii. Thus the covering factor scales as

$$\begin{aligned}
\kappa_{\text{tot}} &\sim M_g(M_h, z) R_{200}(M_h, z)^{-2} \\
&\sim M_h^{1.15} (1+z)^{0.75} M_h^{-2/3} (1+z)^2 \\
&\sim M_h^{0.5} (1+z)^{2.75}, \quad (17)
\end{aligned}$$

where R_{200} is now specified in physical units. This scaling has the proper behavior required to match the absorber statistics considered here: in the cold mode, the covering factor decreases with decreasing mass and increases with redshift. The two gray lines in Figure 7 show this scaling relation for 10^{11} and $10^{10.5} h^{-1} M_\odot$ halos, once again normalized to the model value for $10^{11} h^{-1} M_\odot$ halos at $z = 0.5$. For the best-fit model, the mass and redshift dependence is stronger than in our toy model.

The variables of the model that control the evolution of κ_{tot} in the cold mode are κ_1 , κ_2 , which set the slope of κ_g as a function of halo mass, and β_M . Due to the low contribution to the overall gas cross section from these masses, we are not able to constrain κ_1 and κ_2 tightly. Figure 7b shows $\kappa_{\text{tot}}(z)$ for the same halo masses but for the 2σ upper limit on κ_1 shown in Figure 5. In this model, κ_g scales as $M_h^{0.5}$ at low masses rather than M_h as in the best-fit model. In this realization of our halo model, the scalings of κ_{tot} are in good agreement with the expectations from the toy model. To better constrain these parameters, tighter bias measurements are required—or bias measurements at higher redshift—as well as more precise measurements of $f(W_r)$ at $W_r < 1 \text{ \AA}$.

The presence of an absorber in $M_h \lesssim M_{\text{crit}}$ halos is indelibly linked to the rate of gas accretion. Even if absorbers are caused by active star formation episodes, such episodes cannot occur if there is no fuel coming into the galaxy. If Mg II absorbers are related to star-forming objects it is tempting link the decrease in the cosmic star formation rate from $z = 1$ to $z = 0$ with the measured $n(z)$ for absorbers. Certainly this is the case to some extent; the redshift evolution of Mg II systems is strongest for the highest equivalent widths. But the lack of significant evolution in $W_r < 1 \text{ \AA}$ absorbers argues against such a link for all systems. In addition, $n(z)$ is a cross-section weighted statistic and some care is required for quantitative comparison with the observed star formation rate density.

6.3. Cold gas in hot halos

In the combined model, f_{cold} is $\sim 10\%$. Nominally, this parameter relates to the fraction of cold gas that remains after the halo has been shock heated. In addition to the bias anti-correlation, there are several additional pieces of observational evidence that point to cold gas existing in extended hot gas halos. First, the incidence of Mg II absorbers along lines of sight near $z \sim 0.7$ galaxy clusters is significantly enhanced relative to the field (Lopez et al. 2008). The Lopez et al. (2008) results favor enhancement of stronger absorbers ($W_r \sim 2$) over weaker absorbers, but absorption of any kind reveals the presence of cool gas within the cluster virial radius. Second, the recent measurements of the LRG-Mg II cross-correlation by Lundgren et al. (2009) and Gauthier et al. (2009) extend the previous measurement to small scales— $r < 1 h^{-1} \text{Mpc}$. Pairs at this scale can only be created if LRGs and absorbers exist within the *same halos*; ie, the “one-halo” term from halo models of clustering. Halo occupation analysis of the LRG autocorrelation function constrains LRG halo masses to be $\gtrsim 10^{13} h^{-1} M_\odot$ (Padmanabhan et al. 2008; Blake et al. 2008; Zheng et al. 2008). The multiphase cooling model of Maller & Bullock (2004) predicts that cold clouds are still able to form and survive at halos with virial velocities of 300-400 km s^{-1} , with a cold fraction of 10% at $\sim 320 \text{ km s}^{-1}$. High-resolution hydrodynamic simulations by Kaufmann et al. (2008) support the scenario in which cloud formation is efficient in hot-gas halos with cored density profiles, consistent with the density profile of hot-mode halos in the Kereš et al. (2008) results, which have lower resolution but cosmological volumes.

Detailed analysis of the cross-correlation function of LRGs and Mg II absorbers at both large and small scales can constrain both the covering fraction and density profile of cold gas in hot-mode halos, and this is the subject of ongoing study (J.-R. Gauthier et. al., in preparation).

7. SUMMARY

In this paper, we have used the frequency and abundance of dark matter halos to construct a model for the frequency, abundance, and clustering of Mg II absorption systems. One of the main precepts on which our model is based is the idea of a critical mass scale, below which absorption is high-efficiency and above which absorption is low-efficiency but non-zero. The free parameters of this model are constrained to match the known absorber statistics, allowing us to constrain the relationship between absorption equivalent width and halo mass. Our main findings are:

(1) In order to match the increasing frequency of absorbers with redshift, $n(z)$, the connection between absorbers and dark matter halos must evolve significantly from $z = 0.5$ to $z = 2$. Either gaseous halos must expand with respect to their dark matter radii, or the halo mass range probed by absorbers must expand to account for the data. Different evolutionary scenarios make distinct predictions for the clustering of absorbers at both $z = 0$ and $z \gtrsim 1$.

(2) If M_{crit} remains constant at $10^{11.5} h^{-1} M_\odot$ at all redshifts, the dominant evolutionary mechanism is in the mass of a typical absorber. Strong absorbers are preferentially created in M_{crit} halos at all redshifts, while weak absorbers ($W_r \lesssim 1 \text{ \AA}$) evolve from occupying $10^{13} h^{-1} M_\odot$ halos at $z \lesssim 0.5$ to $10^{11} h^{-1} M_\odot$ halos at $z \gtrsim 1.5$.

(3) In our best-fit model, the cross section of $M \lesssim 10^{11}$ increases significantly from $z = 0$ to $z = 2$. The scaling of $\kappa_g(M)$ with mass and redshift is consistent with a simple picture in which all gas is accreted cold and sinks to the center of the

halo in a freefall time. The increased covering fraction results from higher gas accretion rates and smaller volumes of halos at high redshift.

(4) At $z = 4$, our fiducial model is not able to reproduce the preliminary measurements of the high frequency of absorbers. If these data do not change with greater statistics, this implies that the absorption efficiency of low-mass $M \lesssim 10^{10} h^{-1} M_{\odot}$ is enhanced at these redshifts, or the cross-section around typical galactic halos is expanded beyond their virial radii.

JT would like to thank Ari Maller for useful conversations. JT acknowledges the use of the computational facilities at the Kavli Institute for Cosmological Physics at the University of Chicago. H.-W.C. acknowledges partial support from NASA Long Term Space Astrophysics grant NNG06GC36G and an NSF grant AST-0607510.

REFERENCES

- Abel, T. & Mo, H. J. 1998, *ApJ*, 494, L151+
- Bergeron, J. 1986, *A&A*, 155, L8
- Berlind, A. A. & Weinberg, D. H. 2002, *ApJ*, 575, 587
- Birboim, Y. & Dekel, A. 2003, *MNRAS*, 345, 349
- Birboim, Y., Dekel, A., & Neistein, E. 2007, *MNRAS*, 380, 339
- Blake, C., Collister, A., & Lahav, O. 2008, *MNRAS*, 385, 1257
- Bouché, N., Murphy, M. T., Péroux, C., Csabai, I., & Wild, V. 2006, *MNRAS*, 371, 495
- Brooks, A. M., Governato, F., Quinn, T., Brook, C. B., & Wadsley, J. 2008, submitted, (arXiv:0812.0007)
- Chen, H.-W. & Tinker, J. L. 2008, *ApJ*, 687, 745
- Churchill, C. W., Mellon, R. R., Charlton, J. C., Jannuzi, B. T., Kirhakos, S., Steidel, C. C., & Schneider, D. P. 2000, *ApJS*, 130, 91
- Cooray, A. & Sheth, R. 2002, *Phys. Rep.*, 372, 1
- Dekel, A. & Birboim, Y. 2006, *MNRAS*, 368, 2
- Dekel, A., Birboim, Y., Engel, G., Freundlich, J., Goerdt, T., Mumcuoglu, M., Neistein, E., Pichon, C., Teyssier, R., & Zinger, E. 2008, *Nature*, accepted (arXiv:0808.0553)
- Dunkley, J., Bucher, M., Ferreira, P. G., Moodley, K., & Skordis, C. 2005, *MNRAS*, 356, 925
- Gauthier, J.-R., Chen, H.-W., & Tinker, J. L. 2009, *ApJ*, 702, 50
- Jiang, L., Fan, X., Vestergaard, M., Kurk, J. D., Walter, F., Kelly, B. C., & Strauss, M. A. 2007, *AJ*, 134, 1150
- Kacprzak, G. G., Churchill, C. W., Steidel, C. C., & Murphy, M. T. 2008, *AJ*, 135, 922
- Kaufmann, T., Bullock, J. S., Maller, A., & Fang, T. 2008, in *American Institute of Physics Conference Series*, Vol. 1035, *The Evolution of Galaxies Through the Neutral Hydrogen Window*, ed. R. Minchin & E. Momjian, 147–150
- Kereš, D., Katz, N., Fardal, M., Dave, R., & Weinberg, D. H. 2008, *MNRAS*, submitted (arXiv:0809.1430)
- Kereš, D., Katz, N., Weinberg, D. H., & Davé, R. 2005, *MNRAS*, 363, 2
- Lopez, S., Barrientos, L. F., Lira, P., Padilla, N., Gilbank, D. G., Gladders, M. D., Maza, J., Tejos, N., Vidal, M., & Yee, H. K. C. 2008, *ApJ*, 679, 1144
- Lundgren, B. F., Brunner, R. J., York, D. G., Ross, A. J., Quashnock, J. M., Myers, A. D., Schneider, D. P., Al Sayyad, Y., & Bahcall, N. 2009, *ApJ*, 698, 819
- Maller, A. H. & Bullock, J. S. 2004, *MNRAS*, 355, 694
- Mo, H. J. & Miralda-Escude, J. 1996, *ApJ*, 469, 589
- Nestor, D. B., Turnshek, D. A., & Rao, S. M. 2005, *ApJ*, 628, 637
- Padmanabhan, N., White, M., Norberg, P., & Porciani, C. 2008, *ArXiv e-prints*, 802
- Prochter, G. E., Prochaska, J. X., & Burles, S. M. 2006a, *ApJ*, 639, 766
- Prochter, G. E., Prochaska, J. X., Chen, H.-W., Bloom, J. S., Dessauges-Zavadsky, M., Foley, R. J., Lopez, S., Pettini, M., Dupree, A. K., & Guhathakurta, P. 2006b, *ApJ*, 648, L93
- Rao, S. M., Turnshek, D. A., & Nestor, D. B. 2006, *ApJ*, 636, 610
- Scocimarro, R., Sheth, R. K., Hui, L., & Jain, B. 2001, *ApJ*, 546, 20
- Seljak, U. 2000, *MNRAS*, 318, 203
- Spergel, D. N., Bean, R., Doré, O., Nolta, M. R., Bennett, C. L., Dunkley, J., Hinshaw, G., Jarosik, N., Komatsu, E., Page, L., Peiris, H. V., Verde, L., Halpern, M., Hill, R. S., Kogut, A., Limon, M., Meyer, S. S., Odegard, N., Tucker, G. S., Weiland, J. L., Wollack, E., & Wright, E. L. 2007, *ApJS*, 170, 377
- Steidel, C. C. 1993, in *Astronomical Society of the Pacific Conference Series*, Vol. 49, *Galaxy Evolution. The Milky Way Perspective*, ed. S. R. Majewski, 227–+
- Steidel, C. C. & Sargent, W. L. W. 1992, *ApJS*, 80, 1
- Tinker, J., Kravtsov, A. V., Klypin, A., Abazajian, K., Warren, M., Yepes, G., Gottlöber, S., & Holz, D. E. 2008, *ApJ*, 688, 709
- Tinker, J. L. & Chen, H.-W. 2008, *ApJ*, 679, 1218
- Tinker, J. L., Norberg, P., Weinberg, D. H., & Warren, M. S. 2007, *ApJ*, 659, 877
- Tinker, J. L., Weinberg, D. H., Zheng, Z., & Zehavi, I. 2005, *ApJ*, 631, 41
- Tripp, T. M. & Bowen, D. V. 2005, in *IAU Colloq. 199: Probing Galaxies through Quasar Absorption Lines*, ed. P. Williams, C.-G. Shu, & B. Menard, 5–23
- van den Bosch, F. C. 2002, *MNRAS*, 331, 98
- van den Bosch, F. C., Yang, X., Mo, H. J., Weinmann, S. M., Macciò, A. V., More, S., Cacciato, M., Skibba, R., & Kang, X. 2007, *MNRAS*, 376, 841
- Wechsler, R. H., Bullock, J. S., Primack, J. R., Kravtsov, A. V., & Dekel, A. 2002, *ApJ*, 568, 52
- White, M., Zheng, Z., Brown, M. J. I., Dey, A., & Jannuzi, B. T. 2007, *ApJ*, 655, L69
- Zheng, Z., Coil, A. L., & Zehavi, I. 2007, *ApJ*, 667, 760
- Zheng, Z., Zehavi, I., Eisenstein, D. J., Weinberg, D. H., & Jing, Y. 2008, *ApJ*, submitted, arXiv:0809.1868 [astro-ph]